Supplementary Information

Thermophobic diffusion becomes dominant in ultra-dilute alkali halide aqueous solutions

Shuqi Xu,[1,†] *Kasimir P. Gregory,*[2,3,†] *Alice J. Hutchinson,*[1,2] *Rosemary Zielinski,*[2] *Lincoln D. Hall,*[2] *Ben Corry,*[2,‡,*] *and Juan F. Torres*[1,‡,*]

[1]ANU HEAT Lab, School of Engineering, The Australian National University, Canberra, Australia
[2]Research School of Biology, The Australian National University, Canberra, Australia
[3]School of Science and Technology, University of New England, Armidale, Australia

[†]Co-first authors with equal contribution
[‡]Co-corresponding authors with equal contribution
[*]e-mails: `felipe.torres@anu.edu.au`, `ben.corry@anu.edu.au`

Supplementary Methods

Supplementary Figures

Supplementary Tables

Supplementary Method 1: Experimental measurement of the inversion temperature with digital interferometry

PSI measures the path-averaged refractive index gradient within the Soret cell, which can be attributed to temperature and concentration variations. For ionic solutions, S_T increases with temperature, i.e, ions are thermophilic below T_0 and thermophobic above T_0, which would result in a local maximum of C at T_0. The concentration difference between the initial and end conditions is $\Delta C = \frac{\Delta \Psi'}{\text{OP} \times \text{CF}}$, where OP is the length of the optical path, which is the constant distance that the laser beam travels through the Soret cell, and CF is the contrast factor defined as the refractive index variation with concentration CF $= \delta n / \delta C$. In PSI, CF can be obtained by measuring the phase variation with concentration: CF $= \frac{\Delta \Psi'}{\Delta C \times \text{OP}}$ [1] in an isothermal diffusion experiment, as in Supplementary Fig. 12, where $\Delta \Psi'$ is extracted when ΔC is known or with a refractometer to measure the refractive index variation[2]. Calculation of CF is necessary when using the conventional method of interpolating $S_T(T)$ to find T_0 at $S_T(T_0) = 0$. As the calculation of S_T depends on the measurements ΔC, significant effort has been devoted to measuring the underlying CF, as reported in the literature[2,3]. However, for the method proposed in this work, an important benefit is that obtaining CF is not necessary, as in [1]. OP is a constant determined from the boundaries of the inner walls of the Soret cell. The CF can be treated as constant in an experimental run as the variations of C and T are small. Thus, $\Delta \Psi' \propto \Delta C$. The local maximum of ΔC occurs at the location in which the local maximum (CF is positive) or minimum (CF is negative) of $\Delta \Psi'$ occurs. The experiment sets the Soret cell between the temperature range $[T_{\text{cold}}, T_{\text{hot}}]$, but T_0 is usually not found in the first trial, in which case the temperature is adjusted. Knowing the sign of the contrast factor CF can help determine whether ionic species are thermophobic or thermophilic between $[T_{\text{cold}}, T_{\text{hot}}]$. If thermophilic, the limits of the range $[T_{\text{cold}}, T_{\text{hot}}]$ should be increased in the subsequent trials and vice versa. Recall that quantitative measurement of the exact values of CF is not necessary, only knowing its sign is sufficient. In Supplementary Fig. 12, by means of an isothermal diffusion experiment, we confirm that the sign of $\delta \Psi / \delta C$ is negative for different salts, i.e. $-\Delta \Psi'$ aligns with the increase of C.

Another key point for accurate measurement of the inversion temperature is the distinctively different temperature and concentration development time, which can be characterised by the Lewis number Le $= \frac{\alpha}{D}$. For the five salts used in the experiments[3], Le $\gg 1$ ($50 < $ Le < 130 in temperature range 0–40 °C), which indicates that the temperature development phase can be neglected in the experiments. However, due to the limitation of the PID temperature control device, the temperature difference cannot be applied instantaneously. Supplementary Fig. 6a shows a typical process of the PID temperature variation of the top and bottom boundaries. The time for the PID temperature control to fully stabilise, t_{PID}, is approximately 100 s. The temperature development time, if the boundary temperatures were applied instantaneously, is t_{Tdev}. The background images are taken at time t_{bg} where $t_{\text{bg}} \geq t_{\text{PID}} + t_{\text{Tdev}}$. All reported experimental data were obtained using the Soret cell with a cell height of 4 or 6 mm. Supplementary Fig. 6b shows the effect of temperature and cell height on the normalised time $t_{\text{bg,min}}/\tau$. Supplementary Fig. 6c shows how the measurement of the quasi-linear concentration profile is affected when taking PSI images at different t_{bg} as the background. The later the background image is taken, the larger the concentration error, with the error propagating from the boundaries to the centre of the cell. When $t_{\text{bg}} < 0.03\tau$, the concentration profile is unaffected in the range $0.1h < y < 0.9h$. When $t_{\text{bg}} < 0.06\tau$, the concentration profile is unaffected in the range $0.2h < y < 0.8h$. Therefore, caution should be taken when obtaining T_0 from a local value close to the boundary. Based on Supplementary Fig. 6b and c, for experiments under 20 °C, a Soret cell of height 4 or 6 mm can be used. For experiments above 20 °C, the Soret cell with a height of 6 mm should be used.

Supplementary Method 2: Entropy model of aqueous salt solutions

We developed an entropy model to investigate the thermodynamic behaviour of aqueous salt solutions as a function of concentration, focusing on contributions from ions, hydration shells, and free water molecules. The model employs combinatorial methods from statistical mechanics to capture the configurational and internal entropy changes associated with the solvation process, accounting for the unique properties of different ions. The parameters used in this model are provided in Supplementary Table 2.

Model description

The total entropy (ΔS) of the system is calculated as the sum of the configurational entropy (ΔS_{config}) and the internal entropy ($\Delta S_{internal}$), with an additional clustering entropy term ($\Delta S_{clustering}$) for LiCl solutions, compared to the baseline of bulk water (i.e. $\Delta S = S(C) - S(C = 0)$):

$$\Delta S = \Delta S_{config} + \Delta S_{internal} + \Delta S_{clustering}. \tag{1}$$

1. **Configurational entropy (ΔS_{config}):** This term accounts for the entropy associated with the distribution of different species in the solution, calculated using combinatorial principles. By considering the number of ways to arrange N particles among various species with mole fractions x_i, we apply Boltzmann's entropy formula:

$$\Delta S_{config} = -R \sum_{i}^{N} x_i \ln x_i, \tag{2}$$

   where R is the ideal gas constant. This expression arises from the Stirling approximation of factorials in the combinatorial calculation of microstates[4].

2. **Internal entropy ($\Delta S_{internal}$):** This term represents the entropy due to the internal degrees of freedom (microstates) of each species, incorporating the microstate weights (w_i):

$$\Delta S_{internal} = R \sum_{i}^{N} x_i \ln w_i. \tag{3}$$

   Here, w_i signifies the number of accessible microstates per particle of species i, reflecting differences in internal configurations due to factors like rotational and vibrational modes.

3. **Clustering entropy ($\Delta S_{clustering}$):** LiCl exhibits anomalous behaviour due to its tendency to form ion pairs or clusters at higher concentrations[5]. The clustering increases the number of possible configurations, effectively doubling them for each ion pair, as captured by the $\Delta S_{clustering}$ term:

$$\Delta S_{clustering} = R n_{ion\ pairs} \ln 2, \tag{4}$$

   where $n_{ion\ pairs}$ is the number of ion pairs. This term represents the combinatorial entropy associated with the formation of ion pairs or clusters, acknowledging the additional ways ions can be arranged when clusters form and effectively doubling the number of configurations for each ion pair.

4. **Future extension to clustering entropy ($\Delta S_{clustering}$):** Our current model simplifies the clustering of LiCl into their possible ion-pairs, given the linearity described by Thomas et al[5]. A more generic model for multivalent salt might

need to account for the fraction (α) of ions clustered:

$$\Delta S_{\text{clustering}} = R n_{\text{ion pairs}} \alpha \ln 2, \tag{5}$$

and could further be extended to encompass larger cluster sizes, k, with number of configurations of cluster size k, Ω_k, such that:

$$\Delta S_{\text{clustering}} = R \sum_k n_{\text{k}} \ln \Omega_k. \tag{6}$$

Multi-layered hydration model

The model considers a multi-layered hydration structure around each ion, consisting of:

- **First hydration layer:** Directly coordinated water molecules to the ion, with coordination numbers ($\text{CN}_{\text{cation}}$ and CN_{anion}) that decrease linearly with increasing concentration. The initial coordination numbers are collected from Marcus[6] and have been set to decrease linearly from their initial concentration at a rate of 2.5% per molal, reflecting differences in ionic size.

- **Second hydration layer:** Water molecules in the immediate vicinity beyond the first layer, modelled using a logistic function to account for concentration-dependent occupancy. The number of water molecules in this layer is given by:

$$n_{\text{2nd}} = \frac{n_{\text{2nd(max)}}}{1 + \exp[k(C - C_{\text{mid}})]}, \tag{7}$$

where $n_{\text{2nd(max)}}$ is the number of water molecules in the second layer at $C = 0$, k is a parameter controlling the steepness of the logistic function (set to 2 here), and C_{mid} is the half the saturation concentration. We have avoided the use of the term CN for the 2nd layer, since the term coordination may be a misnomer for the water molecules in this layer. $n_{\text{2nd(max)}}$ was obtained from literature where possible[7,8], however for F^- and I^-, this was approximated from the ratio of the first solvation shell compared to Cl^-:

$$n_{\text{2nd(max)(X)}} = n_{\text{2nd(max) (Cl)}} \frac{n_{\text{1st(max) (X)}}}{n_{\text{1st(max) (Cl)}}}. \tag{8}$$

- **Free water:** Bulk water molecules not associated with the hydration shells. The effective concentration of the bulk water was set to decrease linearly up to saturation. Here the fraction of free water is:

$$\frac{n_{\text{free water}}}{n_{\text{total water}}} = \max\left(0, 1 - \frac{C}{C_{\text{max salt}}}\right). \tag{9}$$

where $C_{\text{max salt}}$ is the saturation concentration of the salt. An alternate might rapidly decrease the free water fraction at low concentration, then slowly trend toward 0 at saturation concentration, with a function $\exp\left[-\left(\frac{C}{C_{\text{max}}}\right)\right]$. However, within this concentration range, it had a negligible effect on the observed behaviour in the linear form. This inherently assumes that if there were enough free water molecules, they could solvate further ions, and hence saturation would not occur. However, they are still feasible, with the caveat that they may be inaccessible or spread out and effectively be trapped from solvating another ion. In this circumstance, the water may not be considered "free" — even if not directly within a solvation shell.

The total number of water molecules is conserved:

$$n_{\text{total water}} = n_{\text{1st}} + n_{\text{2nd}} + n_{\text{free water}}, \tag{10}$$

where

$$n_{1st} = n_{cation}CN_{cation} + n_{anion}CN_{anion}, \tag{11}$$

$$n_{2st} = n_{cation}n_{2nd\ cation} + n_{anion}n_{2nd\ anion}, \tag{12}$$

$$n_{free\ water} = 55.5\frac{n_{free\ water}}{n_{interacting\ water}}. \tag{13}$$

Here, n_{cation} and n_{anion} equate to the concentration for monovalent ions. This will need to be generalised for salts where the valency is different between the cation and anion. Each of the layers is scaled consistently to ensure the total number of water molecules remains the same at all concentrations, given the concentration dependence of each layer has been crudely modelled.

Microstate weights (w_i)

Microstate weights are assigned to each species to represent the number of accessible microstates, influencing the internal entropy:

- **Ions:** The microstate weights for free cations (w_{cation}) and anions (w_{anion}) are ion-specific, reflecting differences in translational freedom and interactions with the solvent. These have been quantified based on the magnitude of the radial charge density of each ion (β)[9], which will govern the strength of its electrostatic interactions:

$$w_{ion} = \frac{0.8}{|\beta_{ion}|}. \tag{14}$$

- **Hydration shells:** The weights for the first ($w_{first\ shell}$) and second ($w_{second\ shell}$) hydration shells account for the restricted movement and ordering of water molecules due to ion-water interactions. The water molecules in the first shell have fewer degrees of freedom compared to those in the second shell. In this model these have been set to:

$$w_{first\ shell} = \frac{1}{|\beta_{ion}|}, \tag{15}$$

$$w_{second\ shell} = \frac{3}{|\beta_{ion}|}, \tag{16}$$

which roughly reflects that the freedom of the water molecules in the first solvation shell are approximately linked to that of the ion, but with some extra rotational degrees of freedom. The second solvation shell has a further increase in both its rotational and translational degrees of freedom and so has a higher weighting.

- **Free water:** Assigned a microstate weight of 1, representing the reference state of maximum entropy for pure water molecules, resulting in lower microstate weights:

$$w_{first\ shell} < w_{second\ shell} < w_{free\ water} = 1. \tag{17}$$

This hierarchy reflects the increasing freedom of water molecules as they move farther from the ion.

Ion-specific effects

- **Cations vs. Anions:** Differences in ionic radius and charge density lead to variations in CN and w_i. Smaller, highly charged ions such as Li^+ and F^- have stronger electrostatic interactions with water molecules, resulting in:

118   – Lower CN due to a smaller available surface area and tighter binding of fewer water molecules.

119   – Reduced w_i for their hydration shells, reflecting more ordered structures with fewer accessible configurations.
120   This has been parameterised by the charge density ρ.

121   The tendency of LiCl to form ion pairs or clusters at higher concentrations and its contribution to $\Delta S_{\text{clustering}}$ has
122   already been discussed in Supplementary Eq. (4).

Assumptions, limitations and potential improvements

124   • **Combinatorial approach:** The model assumes that the entropy can be described using combinatorial methods from
125   statistical mechanics, with particles distinguishable based on their species and state (free ion, hydration shell, free
126   water).

127   • **Linear decrease of coordination numbers:** Coordination numbers decrease linearly with concentration, simplifying
128   the representation of ion-solvent interactions in concentrated solutions. A decrease in coordination number with
129   increasing ion concentration has been shown previously[10], however, these may follow a logarithmic trend rather than
130   linear, and have large error bars that limit the reliability of concentration-dependent fits.

131   • **Ideal mixing:** The solution is considered ideally mixed, and interactions between species are captured through
132   changes in coordination numbers and microstate weights rather than activity coefficients. Indeed, it might be possible
133   that a model such as this could be used to model activity coefficient, but may require degrees of dissociation such as
134   the models proposed by Heyrovska[11], albeit with dynamic coordination numbers and multiple layers.

135   • **Neglect of temperature effects:** The current model is developed at a constant temperature, not accounting for
136   temperature-dependent changes in entropy or enthalpy. Temperature will affect such things as the solubility limit, ion
137   pairing, coordination number, and pH and is an inherently important consideration for thermodiffusive behaviour.

138   • **Identical treatment of cation and anions:** To maintain simplicity, the weightings of cations (w_{cation}) and anions
139   (w_{anion}), as well as the subsequent weightings of their solvation shells, were directly related to their charge density.
140   In reality, this ignores the respective interactions with oxygen and hydrogen, that each have their own unique charge
141   density that will also scale the strength of the electrostatic interactions. Furthermore, hydrogen bonding in anion–
142   water interactions is more directional through the O-H–X^- interaction, in comparison to the O–M^+ interaction,
143   so they will have different changes in degrees of freedom per water molecule that scales differently for anions and
144   cations. Accounting for the partial charge and radii on the oxygen and hydrogen of water for a more thorough
145   electrostatic analysis (such as in Supplementary Fig. 8) might allow for increased generality, especially if the method
146   extends to multivalent ions.

147   • **Uniform microstate weights within layers:** Microstate weights are adjusted based on general trends and are
148   slightly varied for different ions to reflect their unique hydration characteristics, but are assumed uniform within each
149   hydration layer. Representing these to scale electrostatics with distance from the ion, and defining the probabilities
150   of ion-water interactions at each length from a radial distribution function (RDF), as opposed to the coordination
151   numbers in each layer, may better generalise the model. The layer requirements might reduce to a decaying length
152   scale reminiscent of the Debye or Bjerrum length; however, these would still need to be able to account for the water
153   layered observed in RDFs, so would require some oscillatory nature.

154   • **Autoionisation of water:** Under neutral conditions, the concentrations of hydronium (H_3O^+) and hydroxide (OH^-)
155   ions in water are extremely low (approximately $10^{-7}\,\text{M}$). However, even at these trace levels, they could influence the

156   thermodiffusion of alkali halides in ultra-dilute solutions. As alkali halide concentrations approach infinite dilution,
157   H_3O^+ and OH^- concentrations become orders of magnitude higher than those of the salt ions, potentially leading
158   to competition for specific thermal regions. Due to the prohibitive computational costs associated with modelling
159   autoionisation at such low concentrations (by requiring very large system sizes), we did not incorporate it in our
160   FEP simulations. More generally, broadening the scope of this theory to include pH variations could enhance its
161   applicability, allowing for more precise control of thermodiffusion effects[12].

## Connection to thermodiffusion and inversion temperature

The model's entropy calculations can be linked to thermodiffusion phenomena described by Eastman in the late 1920s
[13]. Differences in entropy between solute and solvent contribute to the Soret effect, where a temperature gradient
causes mass transport in a mixture. An increase in the system's entropy with concentration may influence the inversion
temperature—the temperature at which the Soret coefficient changes sign—by altering the balance of thermodynamic
forces. Specifically, if the entropy of the system increases with concentration, a higher inversion temperature might be
required to balance the Gibbs free energy and achieve the sign change in the Soret coefficient.

Conclusion

This entropy model provides a framework for understanding how different ions affect the thermodynamic behaviour of
aqueous salt solutions. By employing combinatorial methods to calculate configurational entropy and considering ion-
specific coordination numbers and microstate weights within a multi-layered hydration structure, the model captures the
essential features of ion solvation and its impact on entropy.
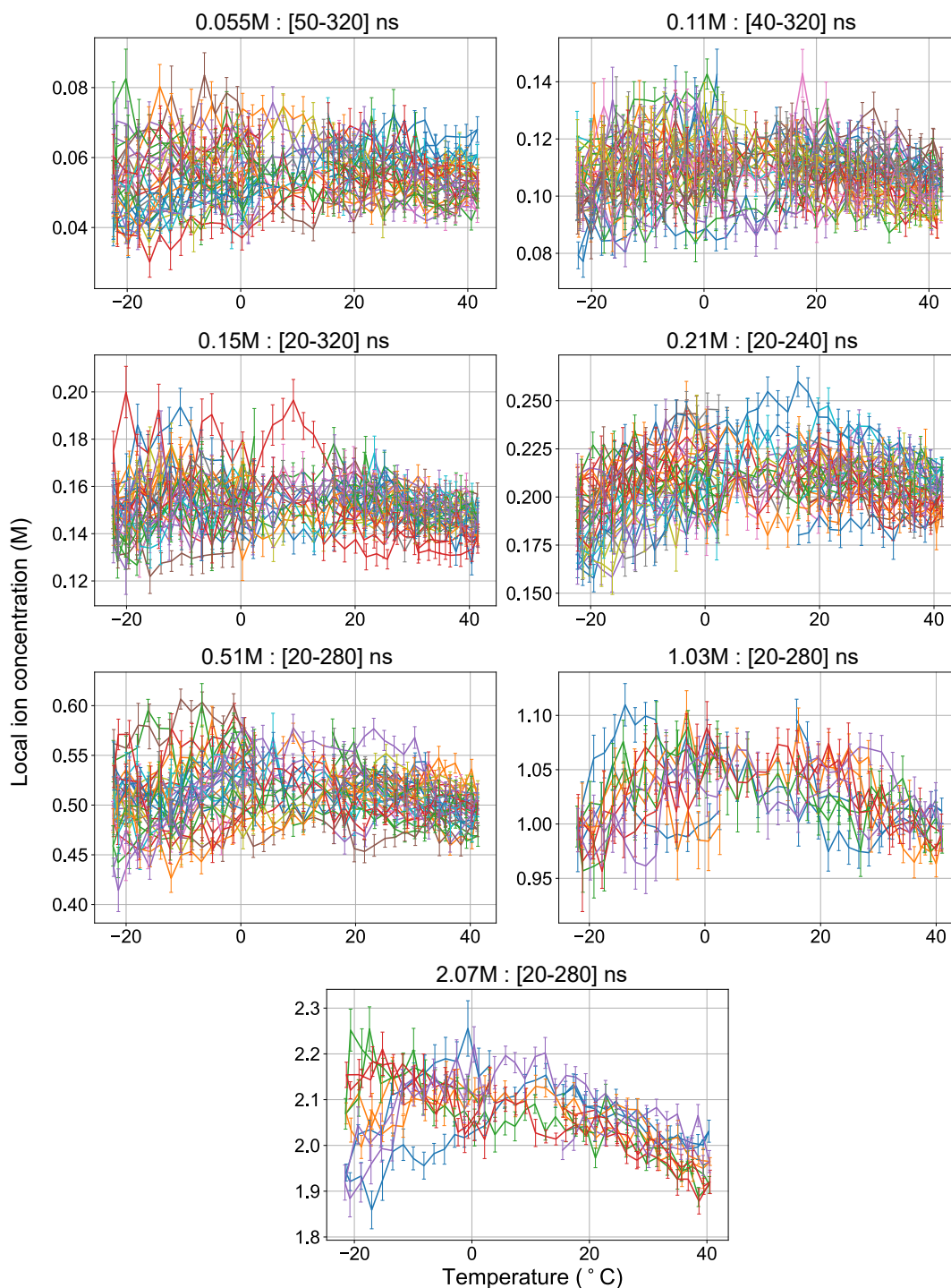
Supplementary Fig. 1 | Noise in the non-equilibrium molecular dynamics (NEMD) simulations. The local ion concentration is plotted across a temperature range. Different colour lines represent different replicates, and the error bars are standard deviations from the time-averaged data. In ascending order from $0.055\,\mathrm{M}$, the number of replicates is 15, 19, 15, 15, 15, 5, and 5, respectively. There is a lot of noise in the data, especially at lower concentrations. The local maximum can be observed visually for $C > 0.2\,\mathrm{M}$. For low concentration simulations, the simulations were run for longer timescales, but the concentration trend is still not clear. This can be statistically accounted for by running more replicates for even longer timescales; however, this becomes computationally very expensive and it can take considerable time for the data to produce meaningful results.
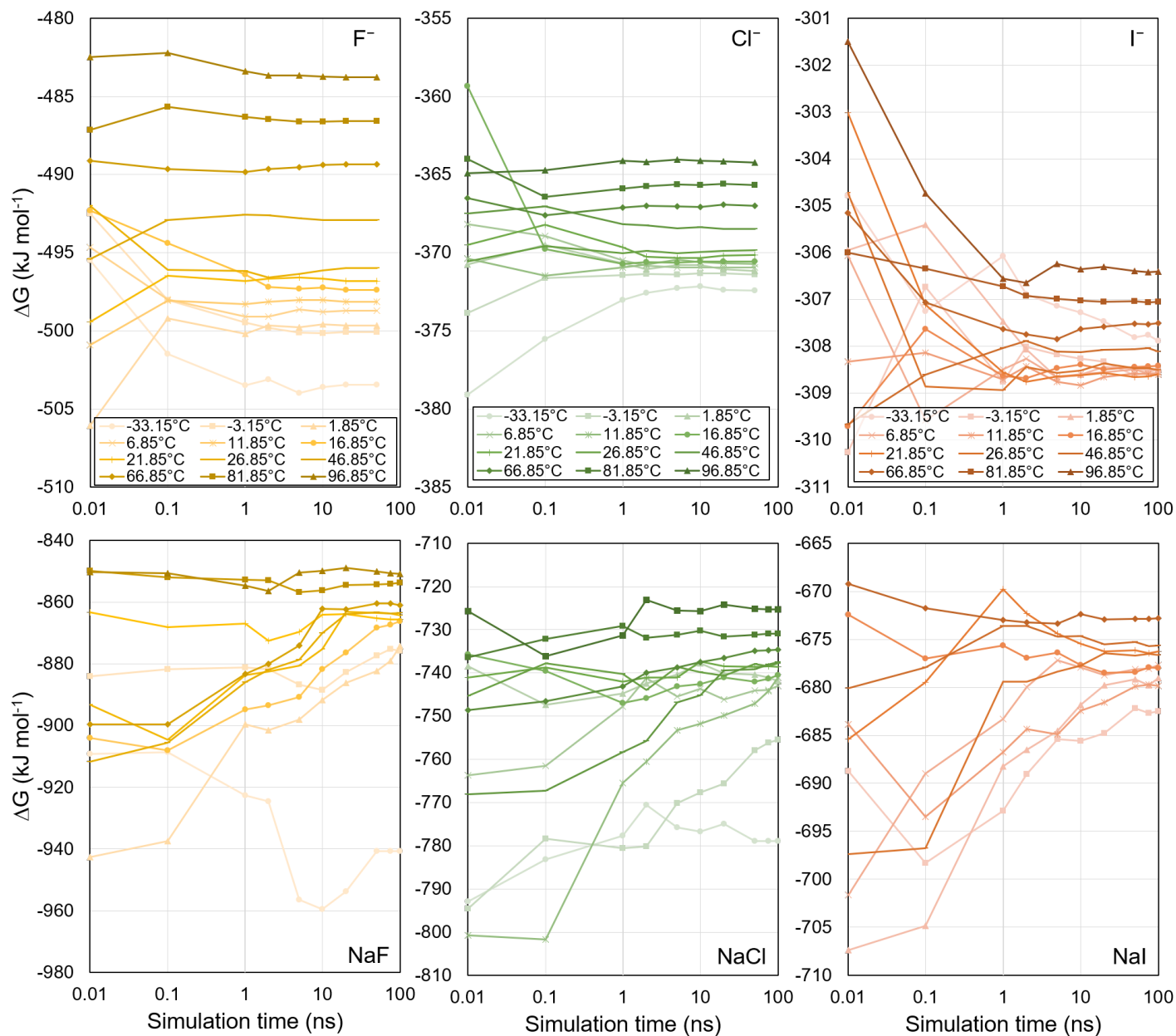
Supplementary Fig. 2 | Convergence of free energy perturbation modelling. The required time lengths of FEP simulations to reach converged results depend on the ion type. Charge-dense ions like F^- were able to converge rapidly, whereas charge-diffuse ions like I^- required longer sampling times. Furthermore, when introducing a salt, where both the cation and anion are simultaneously being tested, even longer timescales are required. This is because they not only have to sample sufficient ion–water configurations, but they also need to sample the ion–ion interactions/distances and the effects these have on the ion–water configurations along the trajectory.
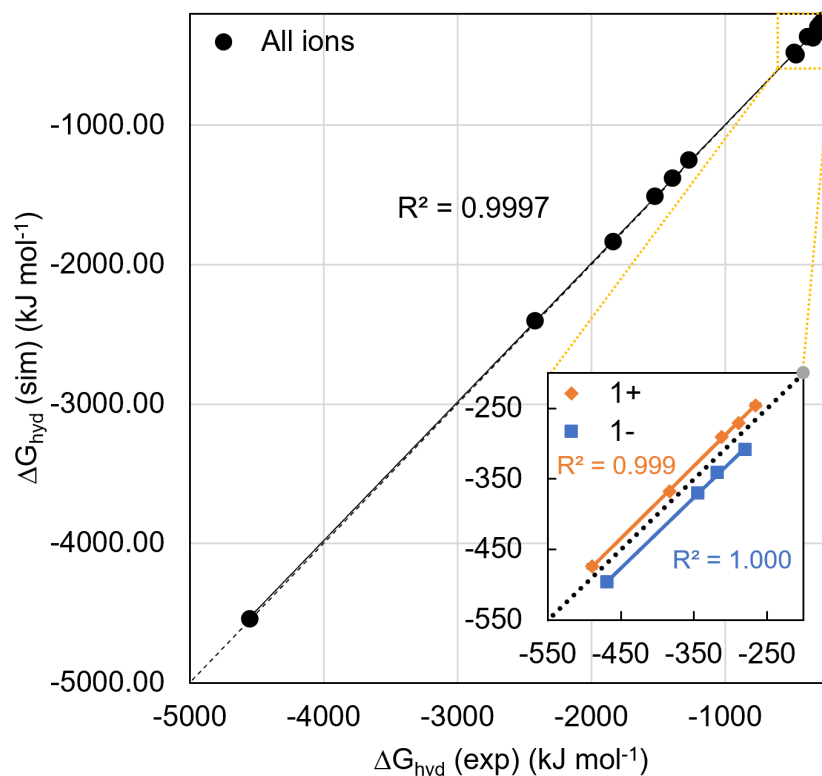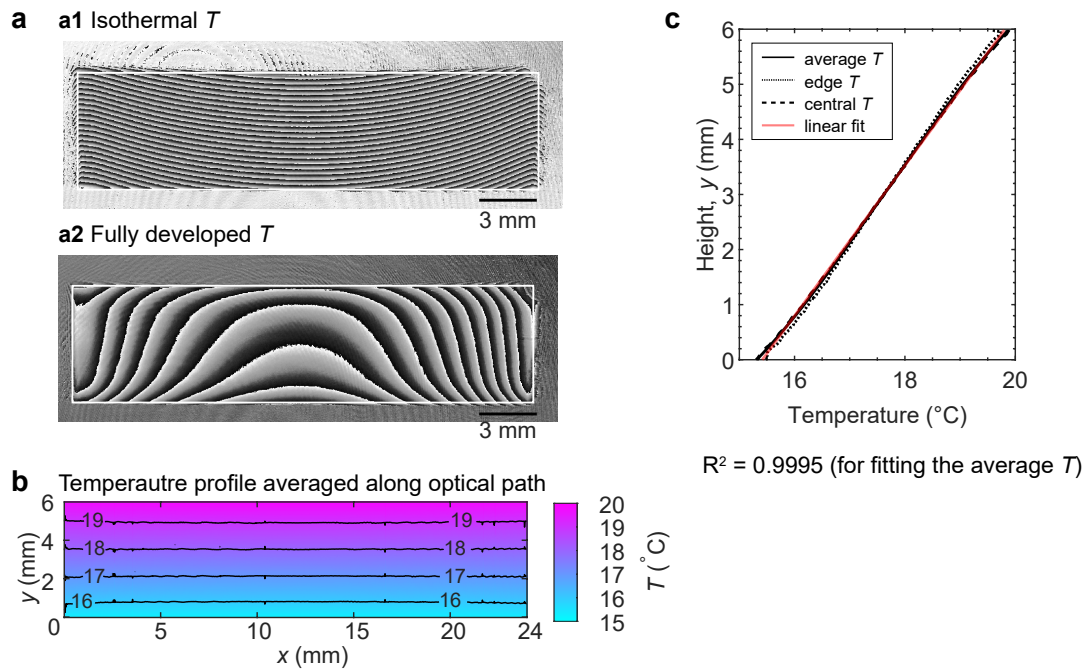
Supplementary Fig. 3 | Comparison of the simulated and experimental free energies of hydration. The ordinate represents the simulated free energy of hydration ΔG_{hyd} (sim), while the abscissa displays the experimental data of ΔG_{hyd} (exp) collated from Marcus[6] from experiments performed at $25\,^{\circ}\text{C}$. The dashed line represents a perfect match between these two sets of data. The ΔG_{hyd} (sim) values at $298.15\,\text{K}$ ($25\,^{\circ}\text{C}$) were extracted from an interpolation of simulated ΔG between 270–$300\,\text{K}$ for each ion. There is a strong correlation between the simulated and experimental Gibbs free energies, indicating that the FEP simulations can represent the trends that arise in specific ion effects for all the ions investigated here (see Supplementary Table 1). The inset shows a slight deviation between the monovalent cations and the anions; the cation ΔG values are overestimated by the simulations while the anions values are underestimated. However, in both cases, this is a systematic deviation, with strong correlations of $R^2 = 0.999$ or greater between the experimental and simulation ΔG values.
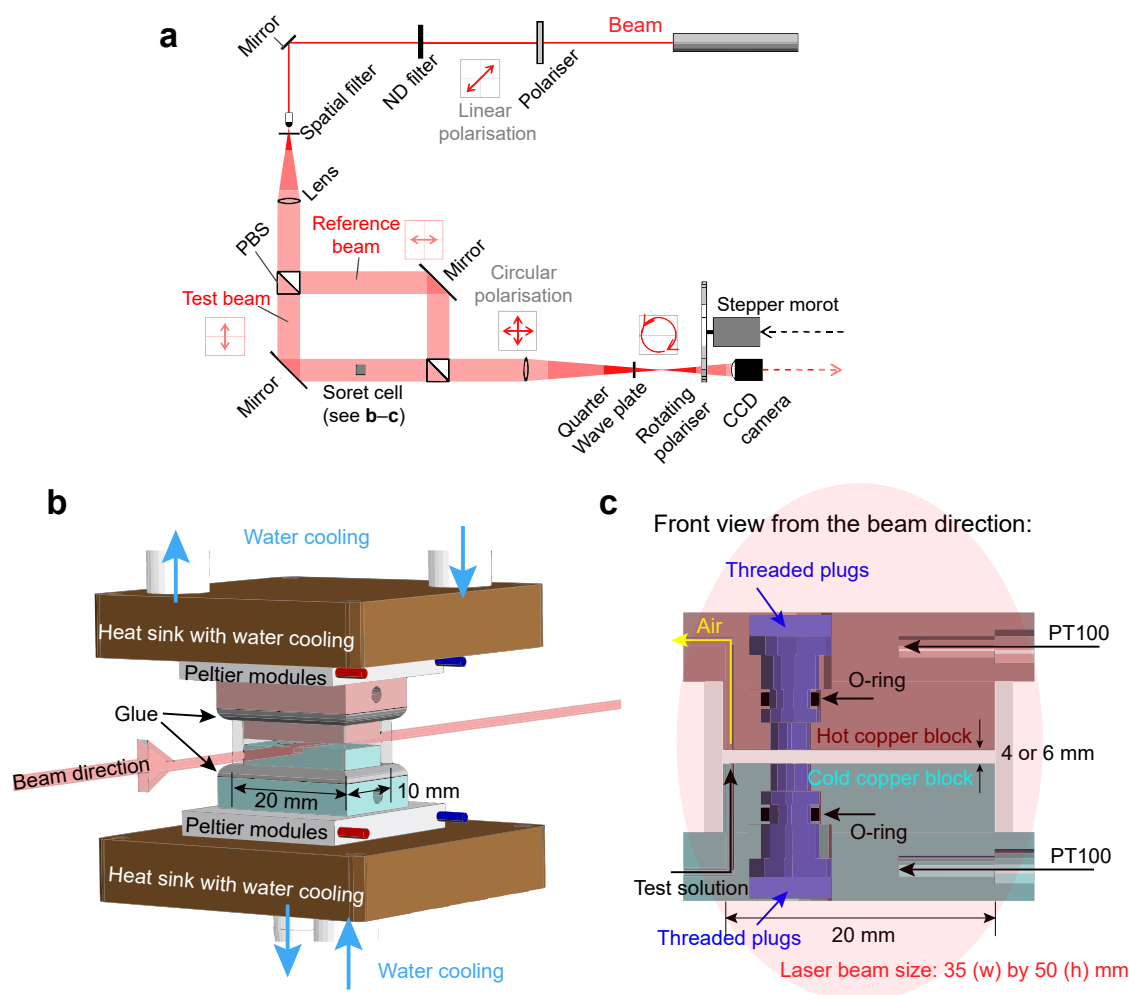
Supplementary Fig. 4 │ **Soret cell used for digital interferometry measurements of inversion temperature**. **a**, The digital interferometry used in the investigation is a temporal phase-shifting interferometry (PSI) technique[14], image adapted from[1] with permission of Elsevier. The Soret cell in **b** is viewed from the indicated arrow direction. **b**, An in-house PID (Proportional–Integral–Derivative) temperature controller is applied to the Soret cell through a pair of PT100 thermistors for temperature measurement and Peltier Modules for active heat flux control. Temperature fluctuations were less than $0.005\,\text{K}$. The heat sinks are immersed in circulating water to allow for fast temperature response, temperature stability in long experiments, and a wide temperature control range. The red arrow indicates the direction (not the entire size) of the laser beam and the optical path within the cell is 10 mm. **c**, The top and bottom of the Soret cell are made of nickel-plated copper to achieve high thermal conductivity without corrosion. The quartz cell is glued to the top and bottom copper blocks to avoid evaporation. The threaded plug allows for thorough cleaning of the Soret cell without removing the glue.

a **a1** Isothermal *T*

a2 Fully developed *T*

3 mm

c

b Temperautre profile averaged along optical path

Supplementary Fig. 5 | Temperature profile within the $6\,\mathrm{mm}$ **high Soret cell. a,** The Soret cell is filled with deionised water to avoid any thermodiffusion-induced concentration difference that interferes with the readings of the temperature profile. Phase-shifted data for isothermal condition (**a1**) and non-isothermal condition (**a2**). Top boundaries is $20.000 \pm 0.001°$C and bottom boundary is $15.000 \pm 0.001°$C. **b,** Contours of the temperature profile based on the known boundary temperatures at the top and bottom, extracted from unwrapping the images in **a**. **c,** Horizontally averaged temperature profiles. Different lines represent different chosen horizontal locations. "edge *T*" is for horizontal location $\in [0.0, 24.0]\mathrm{mm}$, "average *T*" is for horizontal location $\in [0.0, 0.1]\mathrm{mm}$ and $\in [23.9, 24.0]\mathrm{mm}$, and "central *T*" is for horizontal location $\in [0.1, 23.9]\mathrm{mm}$. Linear fit was performed for "average *T*".
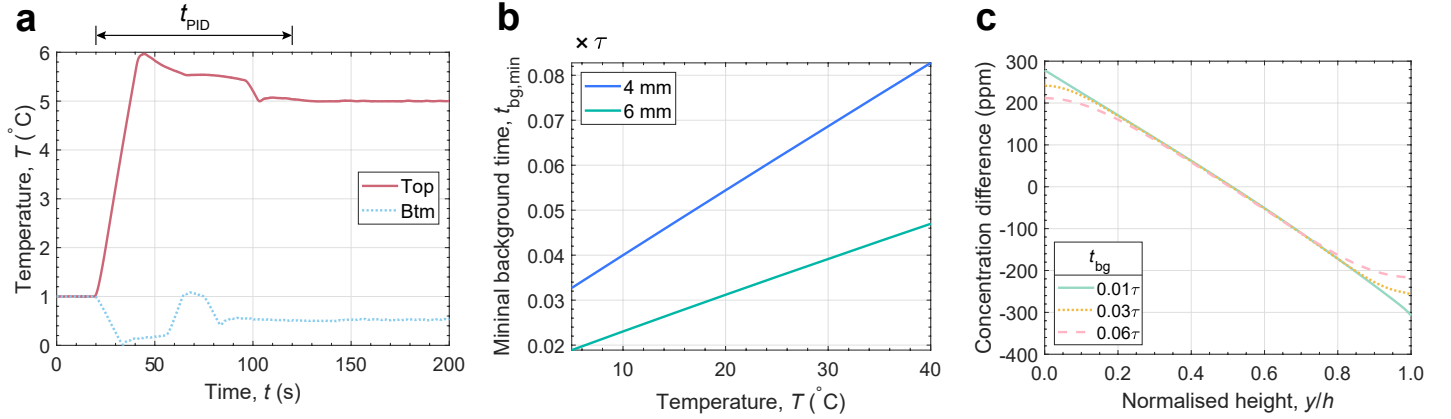
Supplementary Fig. 6 | Loss of concentration information close to Soret cell boundaries. **a**, Temperature change for PID control. It typically takes the PID control $100\,$s to reach the set temperatures and stabilise, which is referred to as t_{PID}. **b**, The minimal background time $t_{\mathrm{bg,min}}$ that guarantees fully-developed temperature profile as a function of temperature T for two different cell heights. $t_{\mathrm{bg,min}} = t_{\mathrm{PID}} + t_{\mathrm{Tdev}}$, which encompasses both the time for PID temperature control to fully stabilise at the set temperatures and the temperature development time ΔT assuming the wall temperature were set instantaneously. **c**, The concentration difference compared to the initial homogeneous stage when taking the background image at the different background time t_{bg}. The actual concentration profile is quasi-linear and large t_{bg} mainly affected the concentration information close to the boundaries.
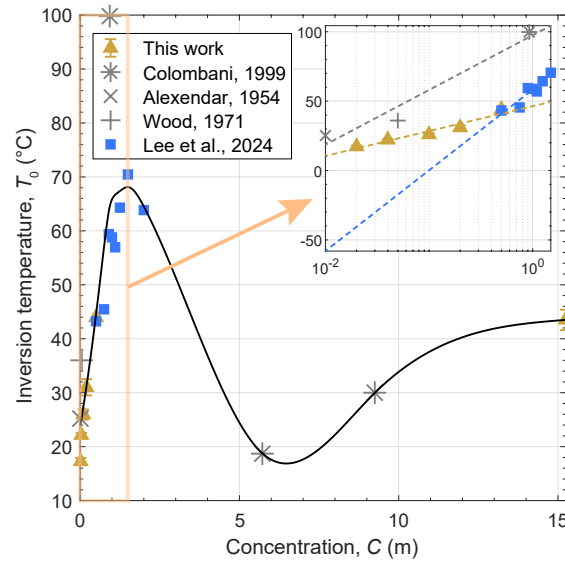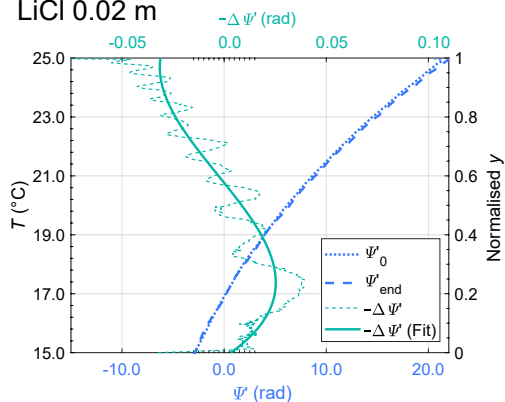

Supplementary Fig. 7 | Inversion temperature for LiCl aqueous solution. "This work" refers to experimental results, same as the LiCl data in Fig. 3. Different literature values were obtained using different methods. "Colombani, 1999" [15], "Alexander, 1954" [16], and "Wood, 1971" [17] were obtained through linear interpolation or extrapolation of $S_{\mathrm{T}}(C)$ data to find the location where $S_{\mathrm{T}}(T_0) = 0$. "Lee et al.,2024" [18] was obtained through interpolation and extrapolation of based on the empirical fit for $S_{\mathrm{T}}(T)$[19] listed in the Supplementary Information of Ref. [18]. The curved black line is a visual guide only. In the inset, the $\log(C)$ plot for $C \in [0.01, 1.5]$m, the dashed lines are linear fits with R^2 values of 0.94, 0.95, 0.88 for "This work"; "Alexander, 1954" and "Wood, 1971" and "Colombani, 1999"; and "Lee et al., 2024", respectively.
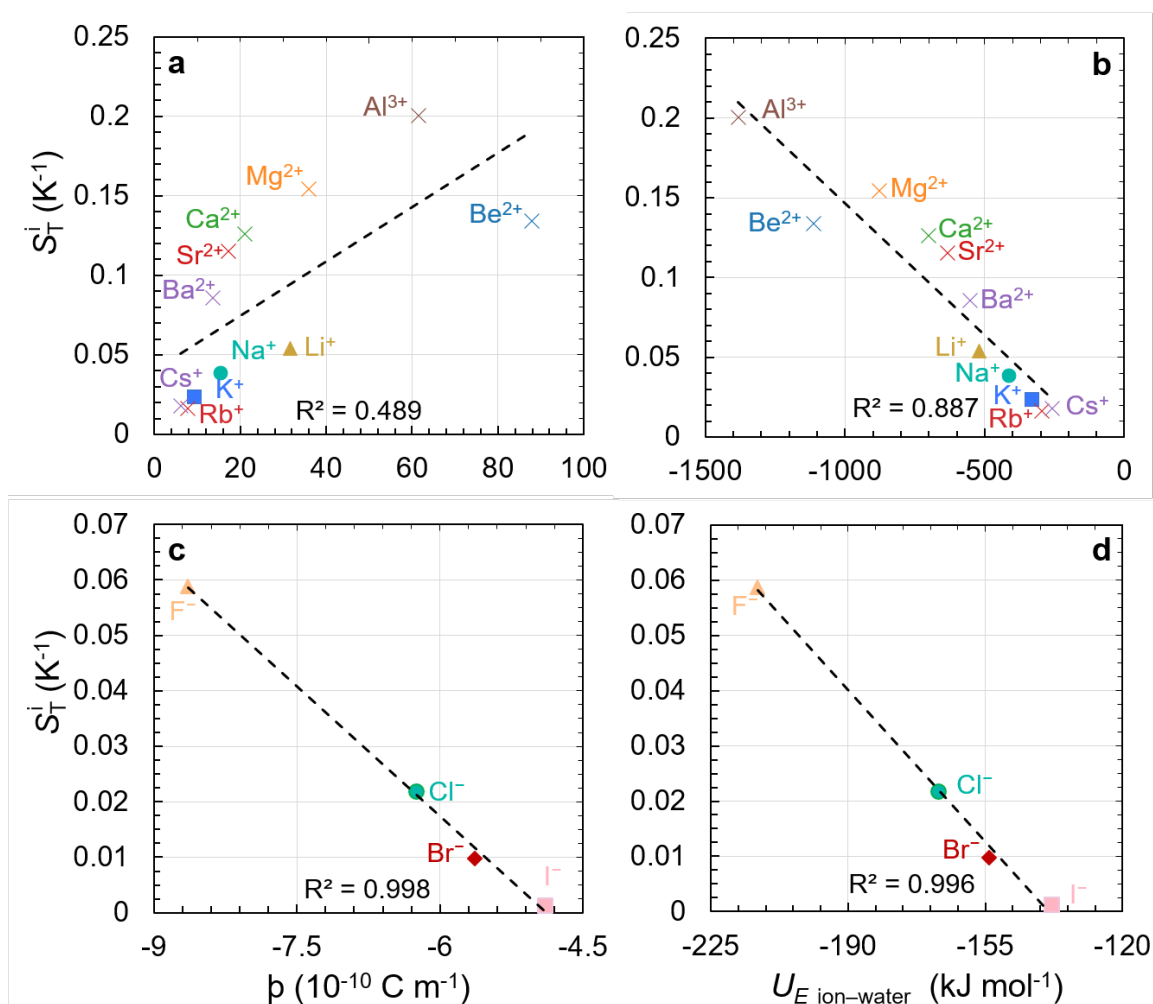
Supplementary Fig. 8 | Lone ion Soret coefficients correlate well with the ion electrostatic properties. The lone ion Soret coefficients S_T^i are calculated using Eq. (2) at $290\,\mathrm{K}$ from the slope of G_{hyd} between $280\,\mathrm{K}$ and $300\,\mathrm{K}$. Although there are reasonable trends with the recent þ parameter (**a**, **c**) for a single valence[9], a more complete electrostatic calculation $U_{E\,\mathrm{ion-water}} = \mathrm{k}_e\,q_{\mathrm{ion}}\,q_{\mathrm{water}}/(r_{\mathrm{ion}} + r_{\mathrm{water}})$ of the interaction (**b**, **d**) with water accounts for differences arising from a change in valence. These results indicate that ions with stronger electrostatic interactions with water are more susceptible to thermal changes due to their higher values of S_T^i. $U_{E\,\mathrm{ion\text{-}water}}$ is derived from Coulomb's law and uses partial radii and charges[9]. These results are inverse to those shown by Duhr and Braun[20] for polystyrene beads and DNA, which had higher Soret coefficients for larger particles; however, these were for particles from one to three orders of magnitude larger than these ions, implying that there may be some critical size (or charge) between these ions and larger particles that reverses this trend. This appears to occur around I^-, the largest of these ions (see Fig. 9), where S_T^i is closest to 0. For I^-, the value of $290\,\mathrm{K}$ is $S_T^i = 0.0012\,\mathrm{K}^{-1}$, less than the kinetic energy term $0.0034\,\mathrm{K}^{-1}$, which is generally treated as negligible[20].
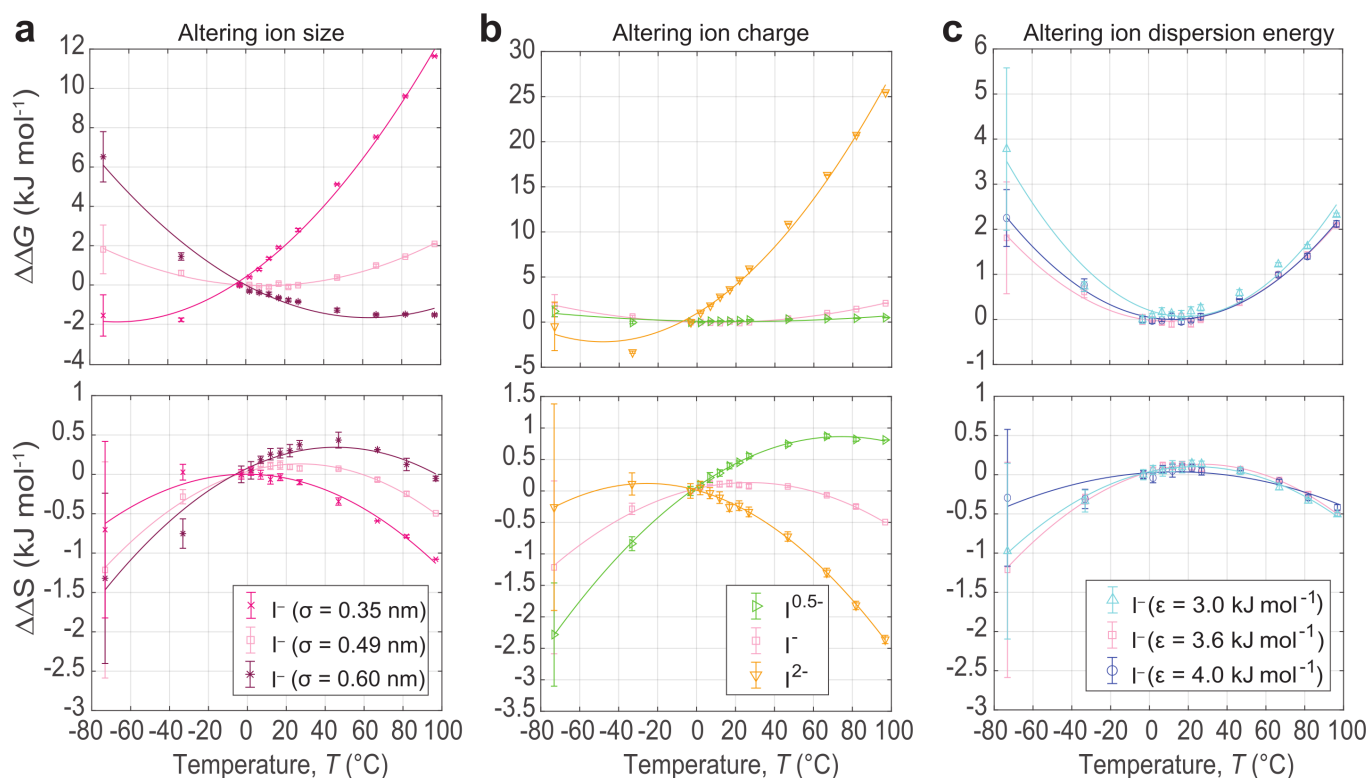
Supplementary Fig. 9 | Effect of altering iodide simulation parameters. The results show that inversion depends on the ions' charge density. To further investigate the origin of the lone ion inversion occurring for the free energy of hydration of lone I$^-$, we tested how altering its parameters affected its $\Delta\Delta G$ (top) inversion as well as $\Delta\Delta S$ (bottom). We altered **a**, the size by changing the sigma parameter, **b**, the charge, and **c**, the dispersion interaction by changing the epsilon parameter. I$^-$ had the original size ($\sigma = 0.49\,\mathrm{nm}$), charge (valency of $1-$) and dispersion interaction ($\varepsilon = 3.6\,\mathrm{kJ\,mol^{-1}}$) parameters from Sengupta et al.[21]. Changing the size appears to have the greatest effect on the inversion temperature of $\Delta\Delta G$ itself, with a complete transition from thermophobic to thermophilic behaviour observed from a small ($\sigma = 0.35\,\mathrm{nm}$) to large altered iodide ($\sigma = 0.60\,\mathrm{nm}$).
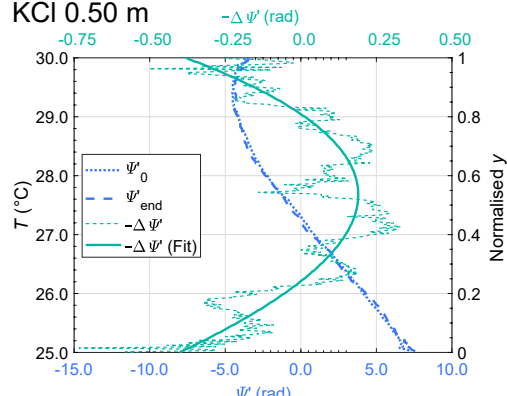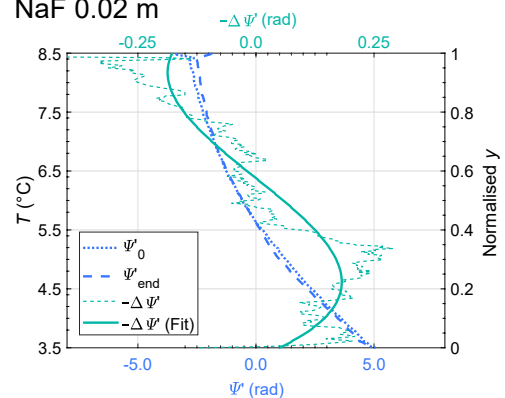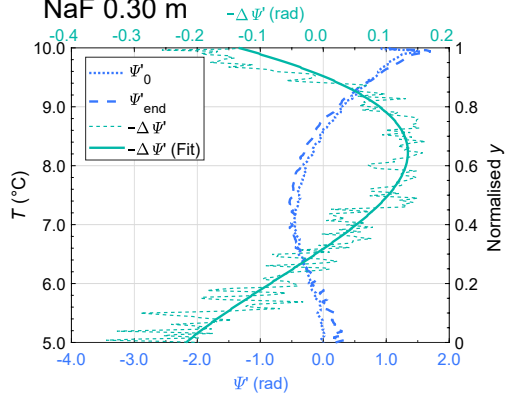
15

a LiCl 0.02 m

LiCl 0.10 m
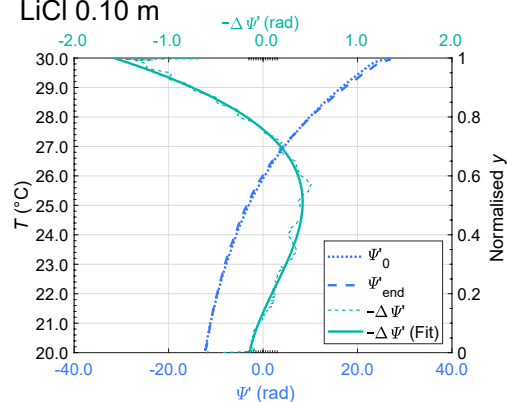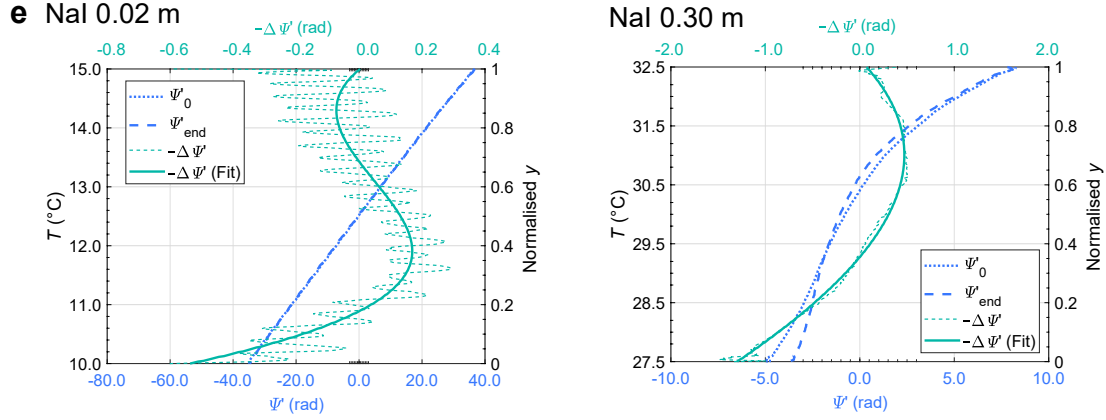
b NaCl 0.02 m
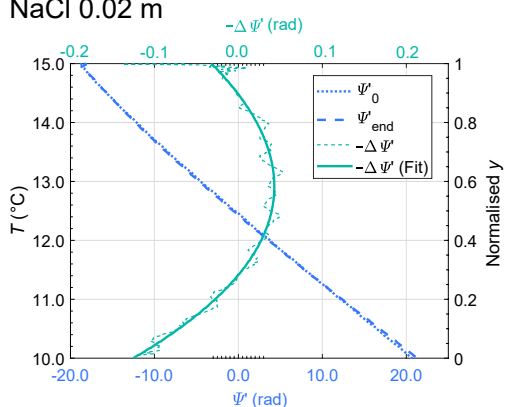
NaCl 0.30 m
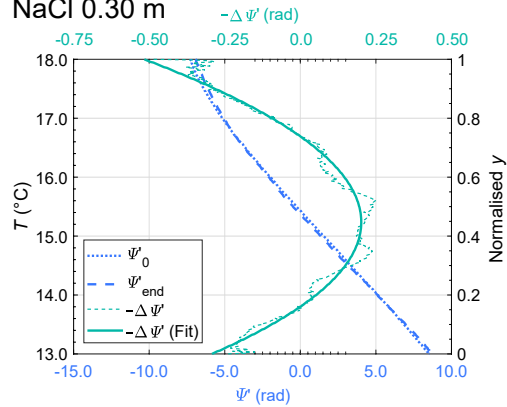
c KCl 0.02 m
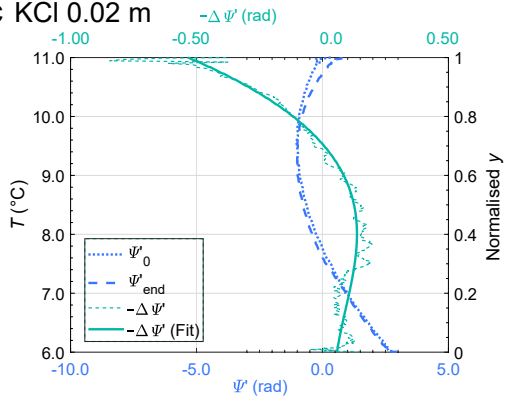
KCl 0.50 m

d NaF 0.02 m

NaF 0.30 m

Supplementary Fig. 10 | Phase-shifting interferometry results for measurements of inversion temperature. **a**, LiCl concentration at 0.02 and $0.10\,\text{m}$. T_0 is 17.32 ± 5.99 and $25.06 \pm 6.69\,°\text{C}$, respectively. **b**, NaCl concentration at 0.02 and $0.30\,\text{m}$. T_0 is 12.87 ± 5.11 and $15.19 \pm 5.87\,°\text{C}$, respectively. **c**, KCl concentration at 0.02 and $0.50\,\text{m}$. T_0 is 8.61 ± 2.49 and $27.62 \pm 182.57\,°\text{C}$, respectively. **d**, NaF concentration at 0.02 and $0.30\,\text{m}$. T_0 is 4.30 ± 2.58 and $8.15 \pm 4.77\,°\text{C}$, respectively. **e**, NaI concentration at 0.02 and $0.30\,\text{m}$. T_0 is 11.97 ± 3.29 and $31.02 \pm 25.05\,°\text{C}$, respectively.
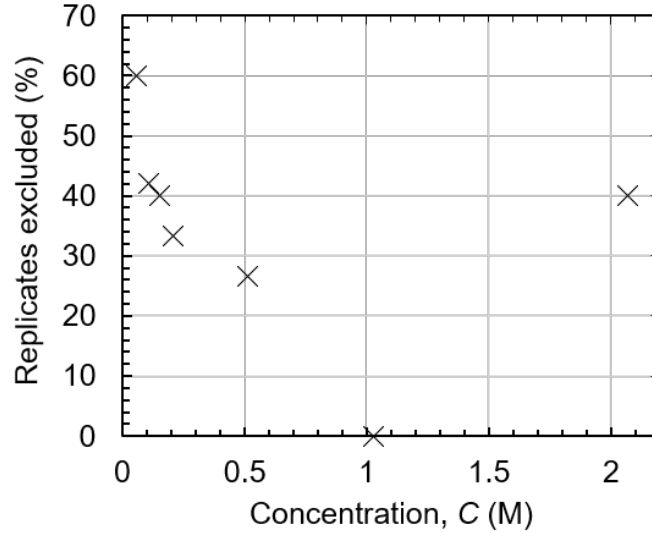
Supplementary Fig. 11 | Percent of replicates with T_0 errors greater than $50\,°\text{C}$ in the NEMD simulations. In general, lower concentration the simulations had a greater proportion of replicates that were not able to be fitted well with $C(T) = C_0 \exp\left\{-S_\text{T}^\infty \left[T + \tau \exp\left(\frac{T_0 - T}{\tau}\right) + k\right]\right\}$ (Ref.[22]) to extract T_0 values with an uncertainty less than $50\,°\text{C}$ (most fits had uncertainties of less than $5\,°\text{C}$). This is likely due to better statistical sampling at higher concentrations.
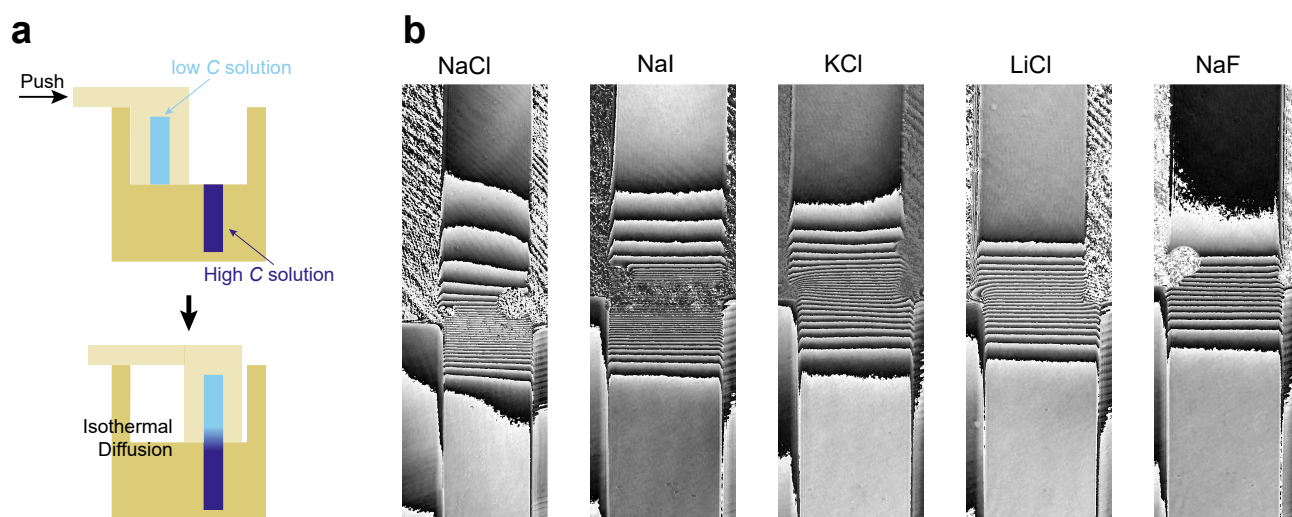
Supplementary Fig. 12 | Isothermal diffusion experiment to confirm contrast factor sign for different salts. a, The isothermal diffusion experiment was done through sliding the top part containing low C solution onto the bottom part containing the high C solution. **b**, Diffusion occurs from the high and low C solution interface. From the top to bottom, the concentration increases while the phase Ψ decreases, i.e. each fringe changes from bright to dark. Thus the contrast factor $\delta\Psi/\delta C$ is negative.
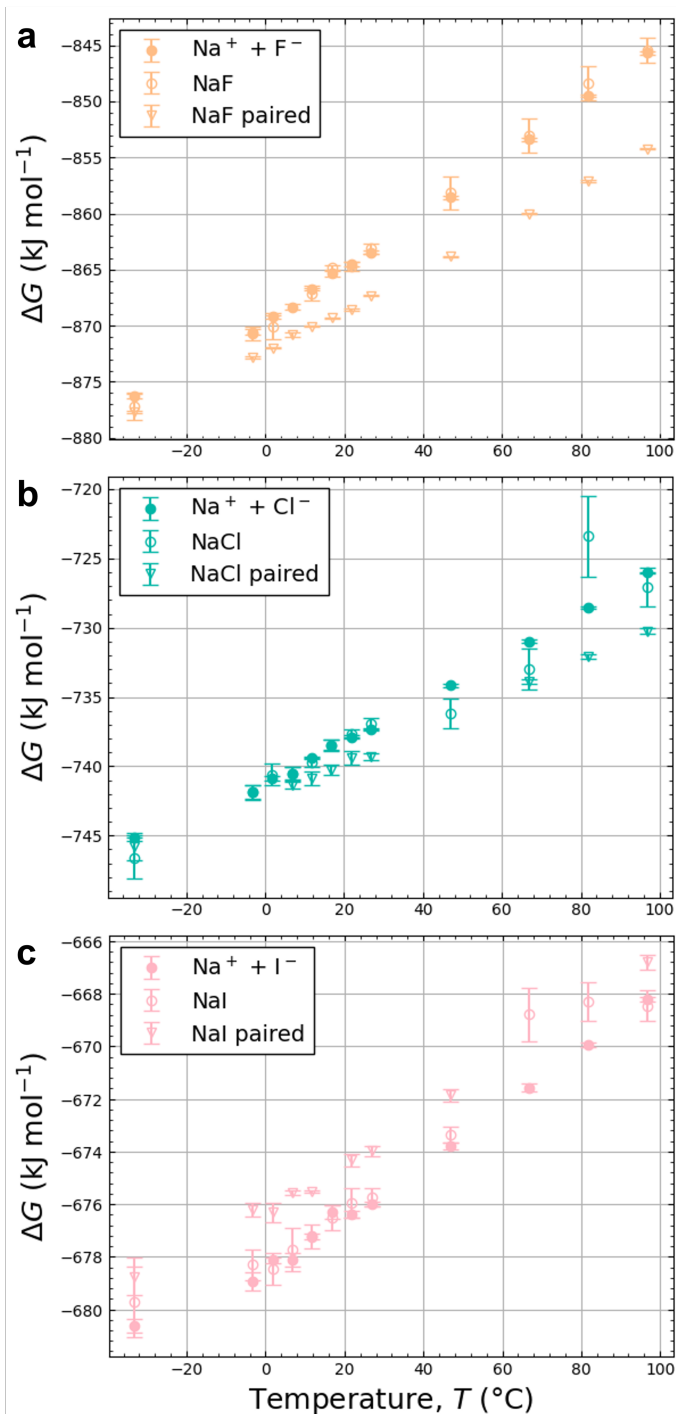
Supplementary Fig. 13 | Effects of having the counterion present and also forcing an ion pair when present. a, The Gibbs free energy of hydration (ΔG) is largely unaffected by measuring the salt separately (i.e. lone Na^+ and lone F^- simulations) or together (i.e. introducing/removing both Na^+ and F^- at the same time in the same simulation). Forcing NaF to be in an ion-pair throughout the simulation increases the magnitude of ΔG, especially at higher temperatures. **b,** Similarly, ΔG is fairly consistent between the lone ions of NaCl and the simulations involving the counterion, with some deviations at higher temperatures. As with NaF, there is a slight increase in the magnitude of ΔG when an ion-pair is forced. **c,** Similarly, ΔG is fairly consistent between the lone ions of NaI and the simulations involving the counterion, with some deviations at higher temperatures as well. However, in contrast to NaF and NaCl, there is a slight decrease in the magnitude of ΔG when an ion pair is forced, with a less clear temperature effect.

Supplementary Table 1 | **Experimental (literature) and simulation (this work) Gibbs energies of hydration**. Standard molar Gibbs energies of hydration experimentally (at $25\,°C$)[6] and via FEP simulations (interpolated to ΔG values at $25\,°C$) with the TIP3P-FB water model[23], monovalent ion parameters from Sengupta et al.[21], di- and tri-valent cation parameters from Li et al.[24,25].

Ion	ΔG_{hyd} (exp) (kJ mol^{-1})	ΔG_{hyd} (sim) (kJ mol^{-1})	ΔS_{hyd} (exp) $(\text{J K}^{-1}\,\text{mol}^{-1})$
		Cations	
Li^+	-489	-473.75 ± 3.36	-141.8
Na^+	-383	-367.71 ± 1.58	-111.2
K^+	-312	-290.35 ± 0.31	-74.3
Rb^+	-289	-270.87 ± 0.60	-65.1
Cs^+	-266	-245.47 ± 3.21	-58.6
Be^{2+}	-2417	-2398.82 ± 5.40	-310.4
Mg^{2+}	-1837	-1833.81 ± 5.40	-331.2
Ca^{2+}	-1527	-1506.51 ± 1.88	-252.4
Sr^{2+}	-1398	-1381.49 ± 6.16	-241.7
Ba^{2+}	-1270	-1249.26 ± 3.46	-208.2
Al^{3+}	-4554	-4542.71 ± 15.13	-538.5
		Anions	
F^-	-469	-496.25 ± 0.76	-137.2
Cl^-	-344	-369.90 ± 0.76	-75.7
Br^-	-318	-341.04 ± 3.41	-58.8
I^-	-280	-308.51 ± 1.02	-35.9

Supplementary Table 2 | **Parameters used in the entropy model for cations and anions**. Parameters for the saturation concentration, C_{max}, radial charge density, þ_{ion}, the initial coordination number of the first solvation shell, CN_{ion}, and second shell, $n_{\text{2nd(max)}}$.

Ion	C_{max} (mol kg^{-1})[26]	þ_{ion} $(10^{-10}\,\text{C m}^{-1})$[9]	CN_{ion}[6]	$n_{\text{2nd(max)}}$
		Cations		
Li^+	19.53 (LiCl)	31.6	4.2	8.0[1]
Na^+	6.14 (NaCl)	15.24	5.4	15[2]
K^+	4.56 (KCl)	9.24	8.3	18.0[3]
		Anions		
F^-	0.96 (NaF)	-8.64	4.6	19.9
Cl^-	6.14 (NaCl)	-6.25	5.6	24.22[4]
I^-	11.81 (NaI)	-4.9	8.0	34.6

Supplementary Table 3 | List of optical elements used in phase-shifting interferometer. The parts are listed below in the direction of the travelling laser.

Part	Part details	Part number	Supplier
He-Ne Laser	632.8 nm, 5 m W, polarised	HNL050LB	Thorlabs
Neutral density filter	Continuously variable ND filter, 50 m m diameter Optical density: 0.04 - 2.0 AR-coated for 350 - 700 nm wavelength	NDC-50C-2M-A	Thorlabs
Linear polarizer	Polymer Film, 25.4 m m diameter Extinction ratio: 700:1 430 - 670 nm	10LP-VIS-B	Newport
Spatial filter	25 μm pinhole and 10$\times$ objective	M900	Newport
Convex lens	2" inch plano-convex lens, $f = 150$ m m AR-coated for 350 - 700 nm wavelength	LA1417-A-ML	Thorlabs
Mirror	2" Protected Aluminum Mirror	PF20-03-G01	Thorlabs
Polarising beamsplitter	2" cube, 420 - 680 nm	PBS519	Thorlabs
Convex lens	2" inch plano-convex lens, $f = 200$ m m AR-coated for 350 - 700 nm wavelength	LA1979-A-ML	Thorlabs
Quarter-wave plate	Zero-Order, Quartz, 25.4 m m diameter, 632.8 nm	10RP04-24	Newport
Linear polarizer	Mounted to stepper motor, 632.8 nm	Custom made	Custom made
CCD Camera	Color CMOS PoE Camera	Manta G-235C	Allied Vision

Supplementary References

1. Torres, J. F., Komiya, A., Shoji, E., Okajima, J. & Maruyama, S. Development of phase-shifting interferometry for measurement of isothermal diffusion coefficients in binary solutions. *Optics and Lasers in Engineering* **50,** 1287–1296 (2012).

2. Gebhardt, M., Köhler, W., Mialdun, A., Yasnou, V. & Shevtsova, V. Diffusion, thermal diffusion, and Soret coefficients and optical contrast factors of the binary mixtures of dodecane, isobutylbenzene, and 1,2,3,4-tetrahydronaphthalene. *Journal of Chemical Physics* **138,** 114503 (2013).

3. Mohanakumar, S., Kriegs, H., Briels, W. J. & Wiegand, S. Overlapping hydration shells in salt solutions causing non-monotonic Soret coefficients with varying concentration. *Physical Chemistry Chemical Physics* **24,** 27380–27387 (2022).

4. McQuarrie, D. A. *Statistical Mechanics* (University Science Books, 2000).

5. Thomas, A. S. & Elcock, A. H. Molecular Dynamics Simulations of Hydrophobic Associations in Aqueous Salt Solutions Indicate a Connection between Water Hydrogen Bonding and the Hofmeister Effect. *Journal of the American Chemical Society* **129,** 14887–14898 (2007).

6. Marcus, Y. *Ions in Solution and their Solvation* 1–293 (John Wiley & Sons, 2015).

7. Bankura, A., Carnevale, V. & Klein, M. L. Hydration structure of salt solutions from ab initio molecular dynamics. *The Journal of Chemical Physics* **138,** 014501 (2013).

8. Liu, H. Y. *et al.* Micro hydration structure of aqueous Li+ by DFT and CPMD. *The European Physical Journal D* **74,** 2 (1 2020).

9. Gregory, K. P., Wanless, E. J., Webber, G. B., Craig, V. S. J. & Page, A. J. The electrostatic origins of specific ion effects: quantifying the Hofmeister series for anions. *Chemical Science* **12,** 15007–15015 (2021).

10. Gregory, K. P., Elliott, G. R., Wanless, E. J., Webber, G. B. & Page, A. J. A quantum chemical molecular dynamics repository of solvated ions. *Scientific Data* **9,** 430 (1 2022).

11. Heyrovská, R. Degrees of dissociation and hydration numbers of alkali halides in aqueous solutions at 25° C (some up to saturation). *Croatica Chemica Acta* **70,** 39–54 (1997).

12. Matreux, T. *et al.* Formation mechanism of thermally controlled pH gradients. *Communications Physics* **6,** 14 (1 2023).

13. Eastman, E. D. Theory of the Soret effect. *Journal of the American Chemical Society* **50,** 283–291 (1928).

14. Torres, J. F., Komiya, A., Henry, D. & Maruyama, S. Measurement of Soret and Fickian diffusion coefficients by orthogonal phase-shifting interferometry and its application to protein aqueous solutions. *Journal of Chemical Physics* **139,** 074203 (2013).

15. Colombani, J., Bert, J. & Dupuy-Philon, J. Thermal diffusion in (LiCl , RH2O). *Journal of Chemical Physics* **110,** 8622–8627 (1999).

16. Alexander, K. F. Zur Theorie der Thermodiffusion in Flüssigkeiten: III. Bestimmung der Soretkoeffizienten von verdünnten wäßrigen Alkalihalogenidlösungen bei den mittleren Temperaturen 30°. 40°, 50° und 60° C. *Zeitschrift für physikalische Chemie (Neue Folge)* **203,** 213–227 (1954).

17. Wood, C. & Hawksworth, W. Thermodiffusion of 1:1 electrolytes in heavy water. *Journal of the South African Chemical Institute* **24,** 170–176 (1971).

18. Lee, N., Mohanakumar, S., Briels, W. & Wiegand, S. Non-monotonic Soret coefficients of aqueous LiCl solutions with varying concentration. *Physical Chemistry Chemical Physics* **26,** 7830–7836 (2024).

19. Iacopini, S., Rusconi, R. & Piazza, R. The "macromolecular tourist": Universal temperature dependence of thermal diffusion in aqueous colloidal suspensions. *European Physical Journal E* **19,** 59–67 (2006).

20. Duhr, S. & Braun, D. Why molecules move along a temperature gradient. *Proceedings of the National Academy of Sciences of the United States of America* **103,** 19678–19682 (2006).

21. Sengupta, A., Li, Z., Song, L. F., Li, P. & Merz, K. M. J. Parameterization of Monovalent Ions for the OPC3, OPC, TIP3P-FB, and TIP4P-FB Water Models. *Journal of Chemical Information and Modeling* **61,** 869–880 (2021).

22. Hutchinson, A. J., Torres, J. F. & Corry, B. Modeling thermodiffusion in aqueous sodium chloride solutions - Which water model is best? *Journal of Chemical Physics* **156,** 164503 (2022).

23. Wang, L.-P., Martinez, T. J. & Pande, V. S. Building Force Fields: An Automatic, Systematic, and Reproducible Approach. *The Journal of Physical Chemistry Letters* **5,** 1885–1891 (2014).

24. Li, Z., Song, L. F., Li, P. & Merz, K. M. J. Systematic Parametrization of Divalent Metal Ions for the OPC3, OPC, TIP3P-FB, and TIP4P-FB Water Models. *Journal of Chemical Theory and Computation* **16,** 4429–4442 (2020).

25. Li, Z., Song, L. F., Li, P. & Merz, K. M. J. Parametrization of Trivalent and Tetravalent Metal Ions for the OPC3, OPC, TIP3P-FB, and TIP4P-FB Water Models. *Journal of Chemical Theory and Computation* **17,** 2342–2354 (2021).

26. Haynes, W. M., Lide, D. R. & Bruno, T. J. *CRC Handbook of Chemistry and Physics* chap. Aqueous Solubility of Inorganic Compounds at Various Temperatures (CRC Press, 2005).

27. Sahle, C. J. *et al.* Hydration in aqueous NaCl. *Physical Chemistry Chemical Physics* **24,** 16075–16084 (26 2022).